

Seismic Velocity Variations in a 3D Martian Mantle: Implications for the InSight Measurements

A.-C. Plesa¹, E. Bozdağ², A. Rivoldini³, M. Knapmeyer¹, S. M. McLennan⁴, S. Padovan¹, N. Tosi¹, D. Breuer¹, D. Peter⁵, S. Stähler⁶, M. A. Wieczorek⁷, M. van Driel⁶, A. Khan⁶, T. Spohn^{1,8}

¹German Aerospace Center (DLR), Berlin, Germany., ²Colorado School of Mines, Golden, CO, USA., ³Royal Observatory of Belgium, Brussels, Belgium., ⁴Stony Brook University, Department of Geosciences, Stony Brook, NY, USA., ⁵King Abdullah University of Science and Technology, Physical Science and Engineering Division, Thuwal, Kingdom of Saudi Arabia., ⁶Institute of Geophysics, ETH Zurich, Zurich, Switzerland., ⁷Université Côte d'Azur, Observatoire de la Côte d'Azur, CNRS, Laboratoire Lagrange, France., ⁸International Space Science Institute (ISSI), Bern, Switzerland.

Contents of this file

1. Comparison of mantle mineralogy for TAY13 and YOS20 compositions
2. Seismic velocities variations
3. Effects of crustal thickness and crustal enrichment
4. Low-velocity zones
5. Ray tracing calculations for YOS20 composition
6. Shadow zone analysis

Additional Supporting Information (Files uploaded separately)

1. Captions for datasets S1 and S2 containing the Perple_X tables for the computation of density and seismic velocities
2. Captions for datasets S3–S8, which include the entire data set of seismic velocities for the hot and cold end-member cases (cases 68 and 65, respectively), as well as for the intermediate case (case 85) for TAY13 (datasets S3–S5) and YOS20 (datasets S6–S8) compositions.
3. Caption for tables S9–S11, which include the shadow zone analysis for all 130 models, TAY13 and YOS20 compositions, and source depths located at 50, 100, and 150 km.

Introduction

In Section S1 we present a direct comparison of the results obtained for TAY13 and YOS20 compositions and discuss the mineral phase proportions that have been obtained for three different thermal states (cases 68 – hot, 85 – intermediate, and 65 – cold end-members). Similar to the main text, we will use here the labels *lowE* (low crustal enrichment) for case 68, *mediumE* for case 85, and *highE* for case 65 in addition to case numbers to mark the difference between the simulations in terms of their total amount of crustal heat production. In Section S2 we show detailed results obtained for a warm end-member (case 68, lowE), a cold end-member (case 65, highE), and an intermediate (case 85, mediumE) temperature profile when using the TAY13 (*Taylor, 2013*) and YOS20 composition (*Yoshizaki and McDonough, 2020*). In Section S3 we present a detailed investigation of the S-wave velocity and its gradient down to 700 km depth for additional models using a different crustal thickness and crustal enrichment than the three end-member models. Section S4 shows the distribution of low-velocity zones for the entire set of 3D thermal evolution models and for both TAY13 and YOS20 compositions. Section S5 shows ray tracing calculations for YOS20 composition to determine the presence of shadow zones, while section S6 presents a shadow zone analysis for the entire set of thermal evolution models.

S1 Comparison of mantle mineralogy for TAY13 and YOS20 compositions

Here we computed the phase proportions below the crust with *Perple_X* using the thermodynamic formulation and thermodynamic database of *Stixrude and Lithgow-Bertelloni (2011)* in order to systematically analyze the differences between the two compositional models (i.e., TAY13 and YOS20). The stable minerals and their proportions are shown for the minimum, average, and maximum temperature profiles for the hot and cold end-member (cases 68 and 65, i.e., lowE and highE cases, respectively) and the intermediate temperature profile (case 85, i.e., mediumE case).

In the lowE model (case 68), which contains most of the HPEs in the mantle and has therefore a high mantle temperature, ringwoodite (ring) and C2/c phases are not stable at high pressure for either thermal profile (minimum, average or maximum). The stability field of garnet and ferropericlase significantly extends at higher pressure (Fig. S1).

The mediumE model (case 85) contains more HPEs in the crust (67.8%) compared to the lowE case (case 68) and has therefore a lower mantle temperature. In this case ringwoodite appears for the TAY13 composition, but only locally (only observed in the minimum temperature profile). For YOS20 composition no ringwoodite appears for any of the temperature profiles (minimum, average and maximum, Fig. S2). For both TAY13 and YOS20 compositions, the orthopyroxene (opx) transforms into the C2/c phase at higher pressure before the stability field of garnet (gt) becomes dominant. However, this is also a local effect that can be seen mainly in the phase proportions for the minimum temperature profile (Fig. S2).

The highE model (case 65) has the lowest mantle temperature, as the HPEs are almost entirely concentrated in the crust and the mantle temperature is about 100 K lower than in case 85 (mediumE). In this case ringwoodite is stable for the (minimum, average and maximum temperature profiles for both compositions. In addition, for both compositions orthopyroxene transforms into C2/c before eventually garnet becomes dominant (Fig. S3).

The increase of the stability field of garnet at the expense of ringwoodite in the TAY13 model has implications for the seismic velocities at the core-mantle boundary (CMB) resulting in a decrease of the seismic velocities. In the hot end-member case (lowE, case 68)

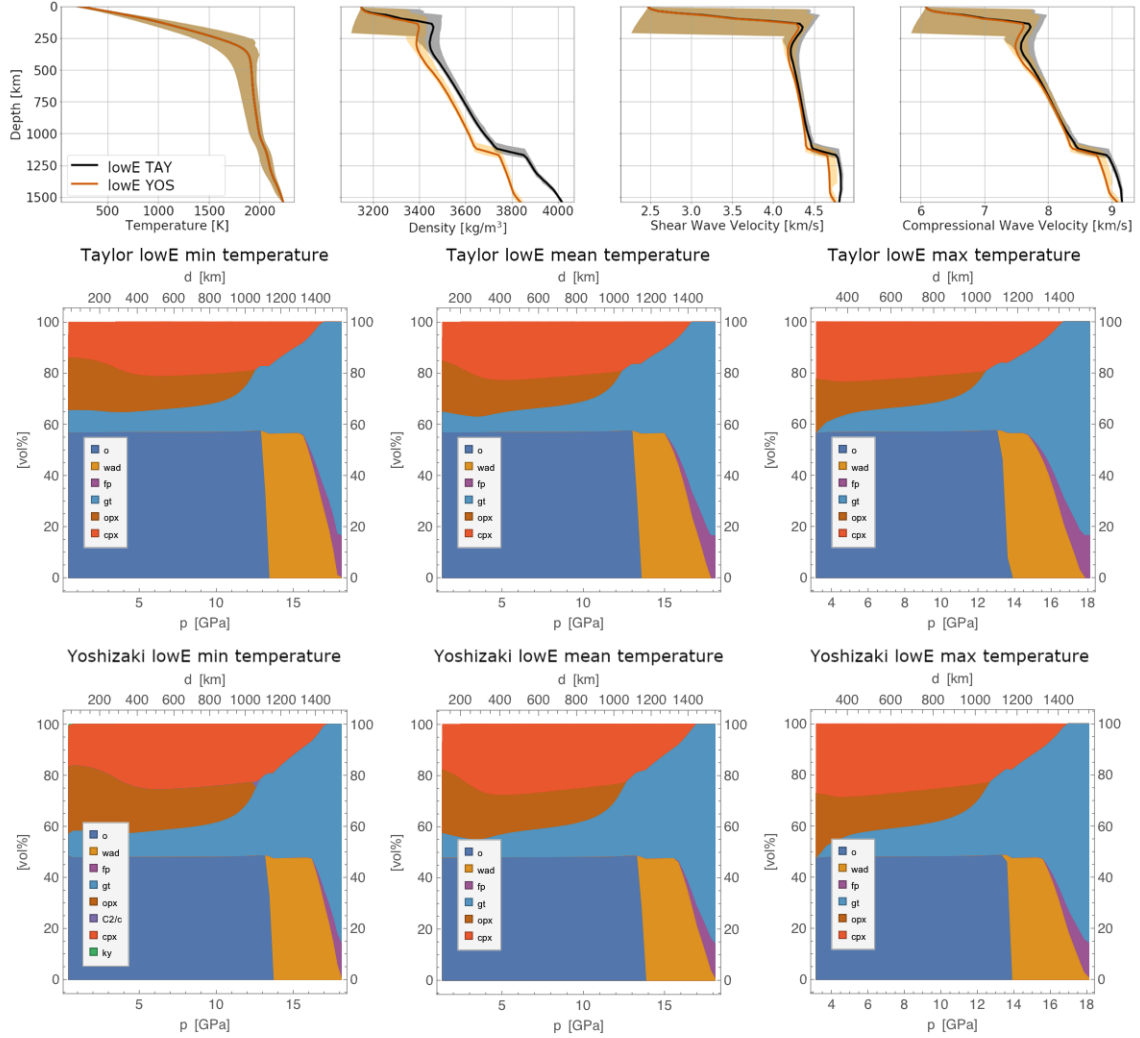


Figure S1: Results of model calculations for the lowE model (case 68 of *Plesa et al.* (2018)) with an average crustal thickness of 87.1 km containing 19.5% of the total bulk amount of HPEs. Top row: Temperature, density and seismic velocities profiles computed for TAY13 and YOS20 compositions. Middle row: Phase proportions for the minimum, average, and maximum temperature profiles computed using the TAY13 composition. Bottom row: Phase proportions for the minimum, average, and maximum temperature profiles computed using the YOS20 composition. Note that the phase proportions are shown below the crust. The mineral assemblage is composed of olivine (o), wadsleyite (wad), ferropericlase (fp), garnet (gt) orthopyroxene (opx), clinopyroxene (cpx), C2/c clinopyroxene (C2/c), and kyanite (ky).

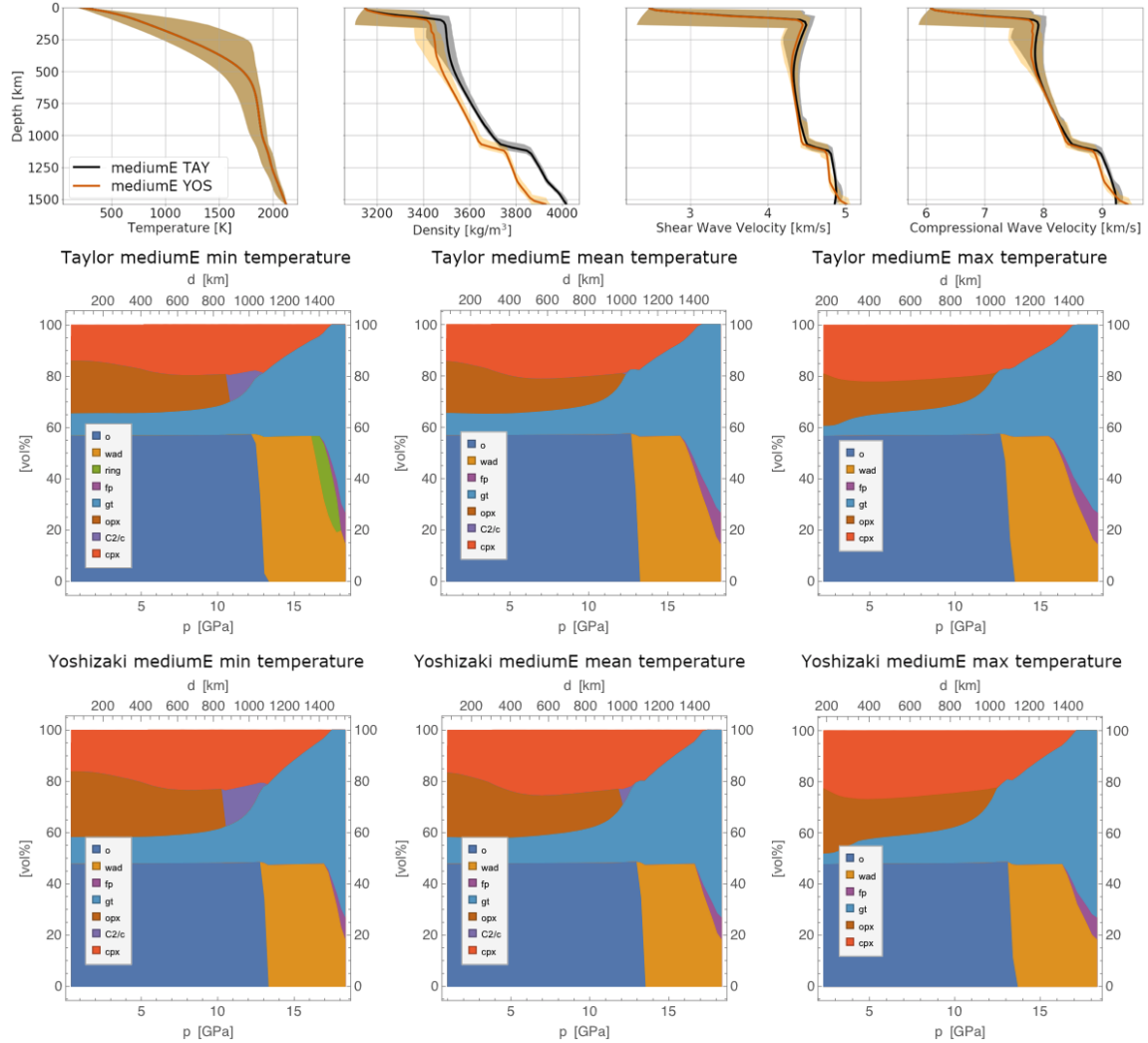


Figure S2: Results of model calculations for the mediumE model (case 85 of *Plesa et al.* (2018)) with an average crustal thickness of 60 km containing 67.8% of the total bulk amount of HPEs. Top row: Temperature, density and seismic velocities profiles computed for TAY13 and YOS20 compositions. Middle row: Phase proportions for the minimum, average, and maximum temperature profiles computed using the TAY13 composition. Bottom row: Phase proportions for the minimum, average, and maximum temperature profiles computed using the YOS20 composition. Note that the phase proportions are shown below the crust. The mineral assemblage is composed of olivine (o), wadsleyite (wad), ringwoodite (ring), ferropericlae (fp), garnet (gt) orthopyroxene (opx), clinopyroxene (cpx), and C2/c clinopyroxene (C2/c).

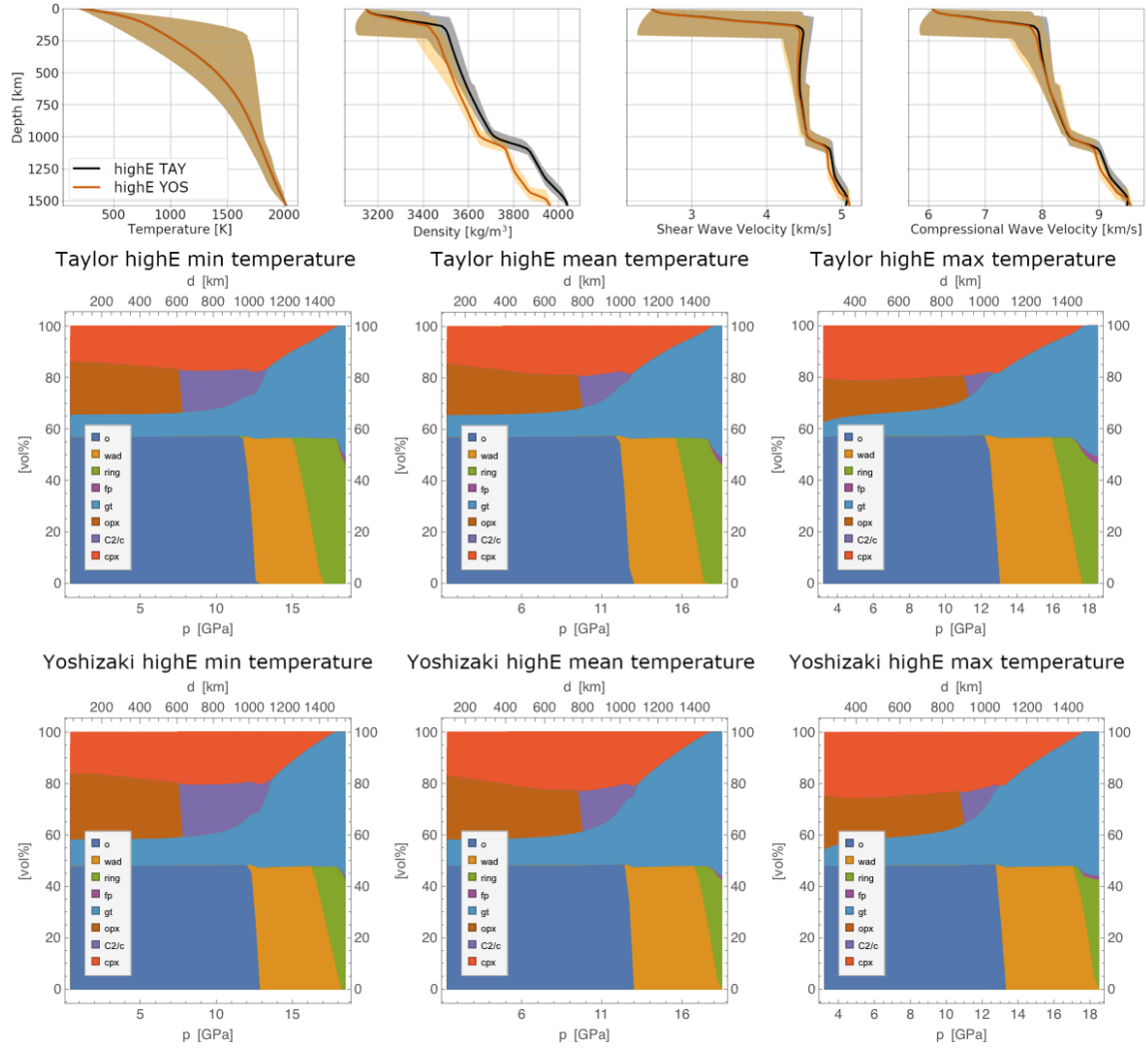


Figure S3: Results of model calculations for the highE model (case 65 of *Plesa et al. (2018)*) with an average crustal thickness of 87.1 km containing 97.6% of the total bulk amount of HPEs. Top row: Temperature, density and seismic velocities profiles computed for TAY13 and YOS20 compositions. Middle row: Phase proportions for the minimum, average, and maximum temperature profiles computed using the TAY13 composition. Bottom row: Phase proportions for the minimum, average, and maximum temperature profiles computed using the YOS20 composition. Note that the phase proportions are shown below the crust.

ringwoodite is not stable. At depths larger than about 1450 km, ferropericlase and garnet are the only mineral phases present, with the amount of ferropericlase slightly increasing with depth but garnet remaining the dominant phase (Fig. S1). In this case the seismic velocities close to the CMB for the TAY13 composition show only a slight decrease compared to the layers immediately above and is caused by the increasing amount of ferropericlase. In the YOS20 composition the decrease of the seismic velocities close to the CMB is not observed. This is partly because of the lower amount of ferropericlase and partly because of the lower FeO content that affects the velocities of those phases. The differences at the CMB between TAY13 and YOS20 become more accentuated in the intermediate and cold end-member scenarios. In the intermediate temperature case (mediumE, case 85), ringwoodite becomes stable for the TAY13 composition only for the minimum temperature profile (coldest local mantle temperatures, Fig. S2). This increases locally the seismic velocity when the ringwoodite phase appears (visible only for the maximum seismic velocities shown by grey shaded areas). The seismic velocities drop locally when the ringwoodite phase is no longer stable. This behavior is not observed for the YOS20 composition, as in this case no ringwoodite is present. For the cold end-member temperature case (highE, case 65), ringwoodite is stable in the deep mantle for all three temperature profiles (minimum, average and maximum profiles). The stability of garnet and ferropericlase at the expense of ringwoodite is clearly observed for the TAY13 seismic velocities close to the CMB, being characterized by a negative seismic velocity gradient. The abrupt increase of the amount of garnet and ferropericlase phases close to the CMB in the TAY13 model is responsible for this behavior. In the YOS20 composition, the decrease of the amount of ringwoodite, and increase of the stability of garnet and ferropericlase is less pronounced close to the CMB compared to TAY13 (Fig. S3). This behavior together with the lower amount of Fe prevent a negative seismic velocity gradient for the YOS20 composition.

S2 Seismic velocities variations

A more detailed illustration of the effects of the thermal state of the interior for the Taylor (*Taylor, 2013*) and Yoshizaki (*Yoshizaki and McDonough, 2020*) compositional models is shown in Fig. S4 – S7. In addition to the information presented in Fig. 3 of the main manuscript, we also show the variations of the lithospheric thickness (Fig. S4 and S6).

A thick crust highly enriched in HPEs accentuates the differences in temperature and lithospheric thickness between the regions covered by a thin and a thick crust, and hence leads to the largest lithospheric temperature and lithospheric thickness variations (Fig. S4a, highE). On the other hand, the lithospheric thickness and lithospheric temperature variations are the least pronounced for a crust that is only slightly enriched in HPEs compared to the mantle (Fig. S4a, lowE).

Fig. S5 and S7 show a detailed distribution with depth of both S-wave velocity and its gradient in the uppermost 700 km. The distribution of seismic velocities in the upper part of the mantle is similar between the two compositions. Slight differences can be observed for the S-wave velocity gradient. While only parts of the southern hemisphere show a positive S-wave velocity gradient at 500 km depth for mediumE and highE models (cases 85 and 65, respectively) for TAY13 composition, for the YOS20 composition the S-wave velocity gradient is positive over the entire southern hemisphere at the same depth (cf. Fig. S5 and S7). However, these difference are minor. Additionally the phase transition from orthopyroxene (opx) to C2/c starts at a slightly deeper depth and is slightly less pronounced for the TAY13 composition compared to the YOS20 composition (compare also the mineral

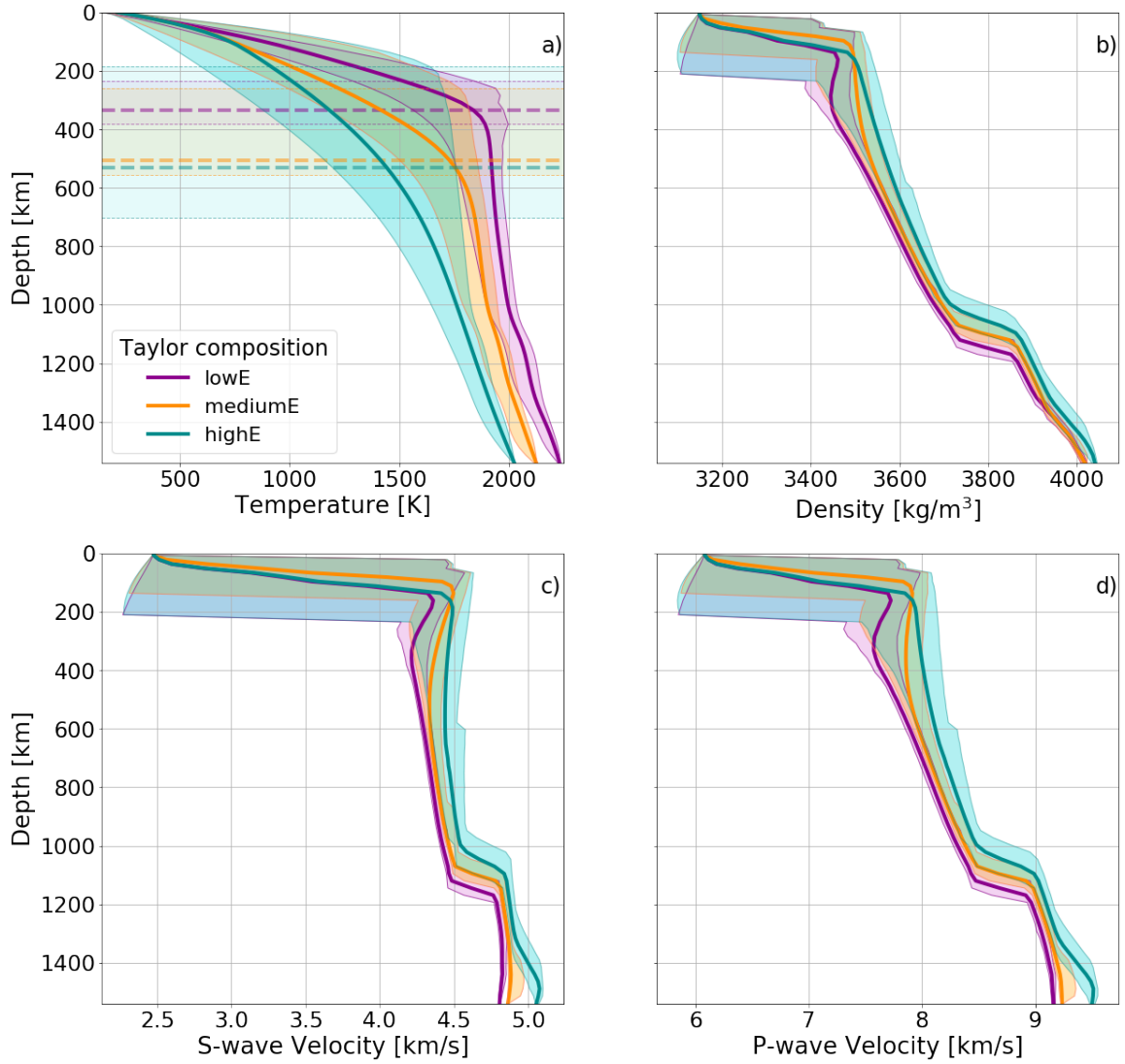


Figure S4: Results of model calculations comparing the mantle composition of Taylor (*Taylor, 2013*) for the lowE, mediumE, and highE models (cases 68, 85, and 65, respectively, of *Plesa et al. (2018)*). The full lines show the average profiles of a) temperature, b) density, c) S-wave velocity, and d) P-wave velocity. The shaded envelopes show the variations at each depth. The average lithosphere thickness is indicated by horizontal dashed lines while lithosphere thickness variations are shown by horizontal shaded areas in panel a. For the crust we used the composition discussed in *Taylor and McLennan (2009)*.

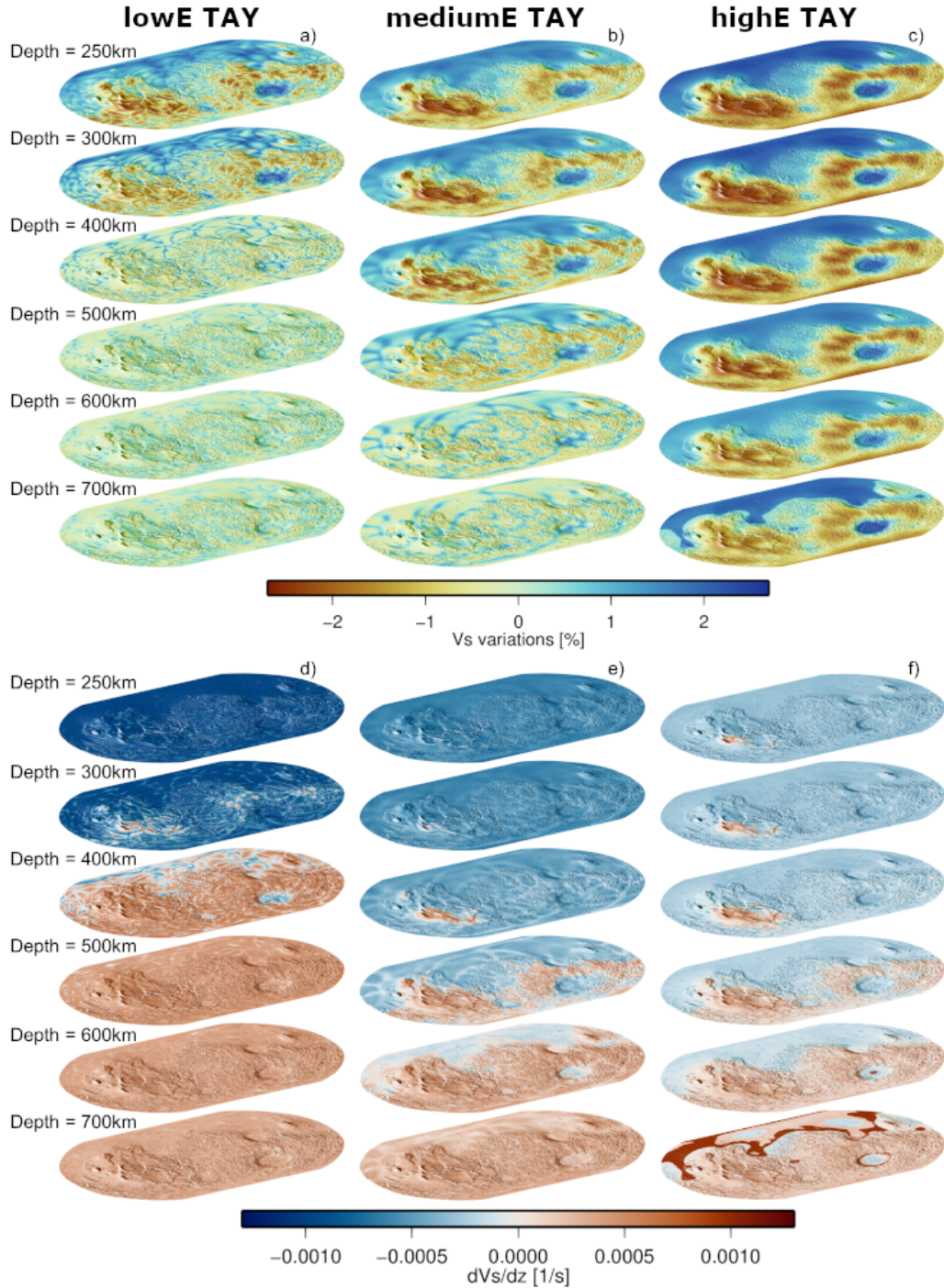


Figure S5: Top panels: seismic velocity variations as a function of depth: a) lowE (case 68), which employs a crust with an average crustal thickness of 87.1 km containing 19.5% of the total bulk amount of HPEs; b) mediumE (case 85), which employs a crust with an average crustal thickness of 62 km containing 67.8% of the total bulk amount of HPEs; c) highE (case 65), which employs a crust with an average crustal thickness of 87.1 km containing 97.6% of the total bulk amount of HPEs. Bottom panels: corresponding S-wave velocity gradient. The mantle compositional model used here is TAY13 (*Taylor, 2013*). Note that the color scale is saturated for the largest S-wave velocity gradient.

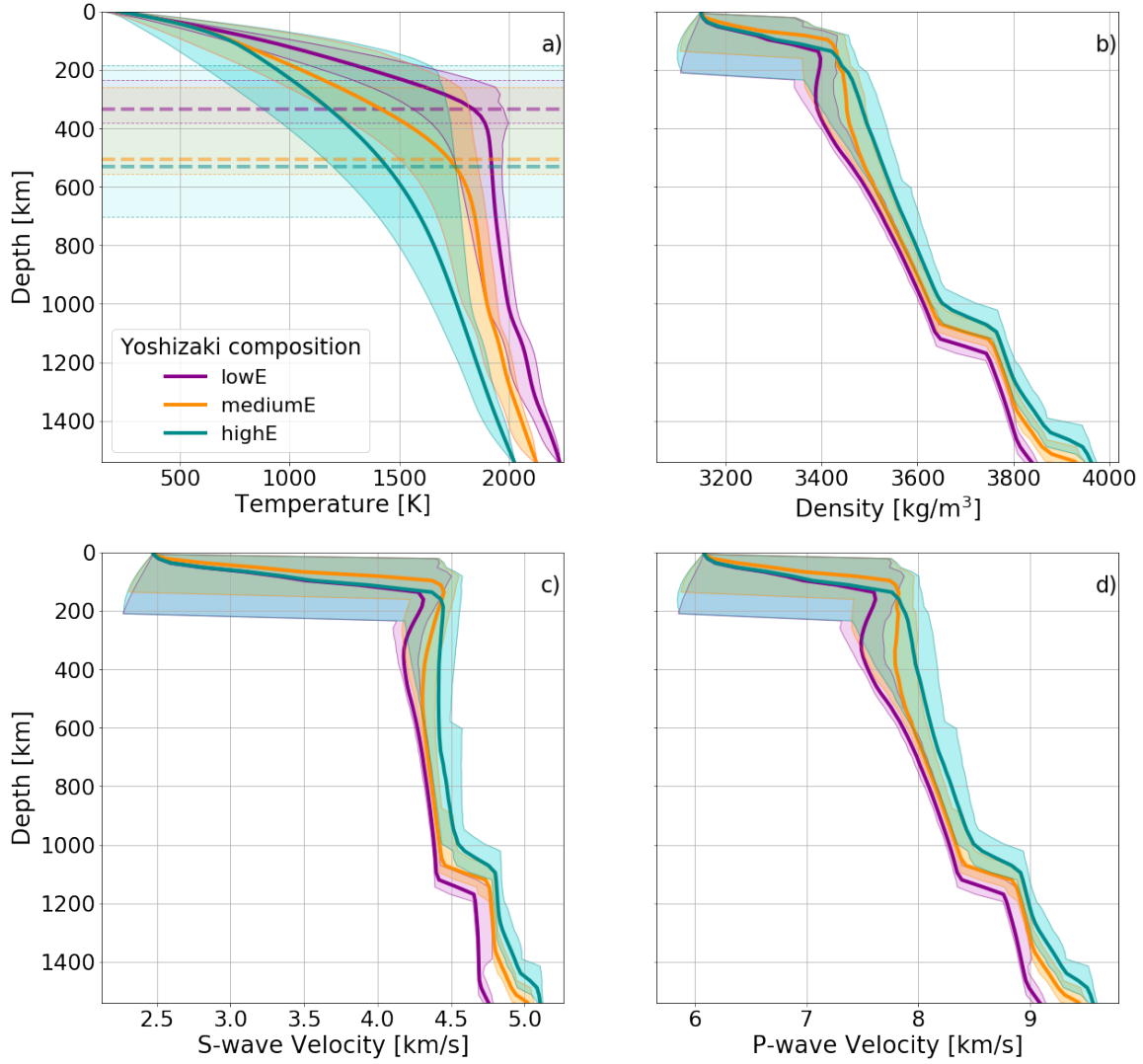


Figure S6: Results of model calculations comparing the mantle composition of Yoshizaki (*Yoshizaki and McDonough, 2020*) for the lowE, mediumE, and highE models (cases 68, 85, and 65, respectively, of *Plesa et al. (2018)*). The full lines show the average profiles of a) temperature, b) density, c) S-wave velocity, and d) P-wave velocity. The shaded envelopes show the variations at each depth. The average lithosphere thickness is indicated by horizontal dashed lines while lithosphere thickness variations are shown by horizontal shaded areas in panel a. For the crust we used the composition discussed in *Taylor and McLennan (2009)*.

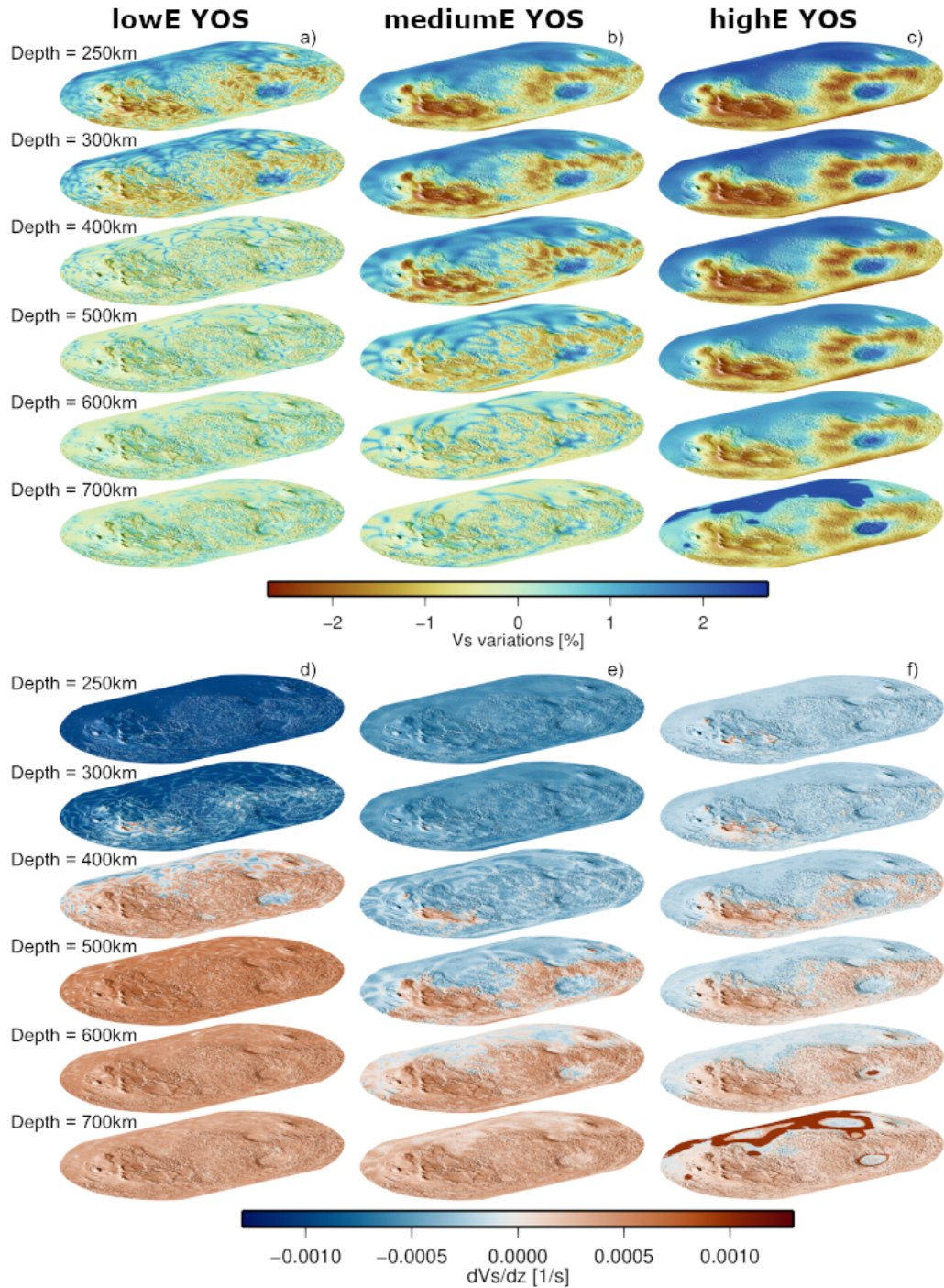


Figure S7: Top panels: seismic velocity variations as a function of depth: a) lowE (case 68), which employs a crust with an average crustal thickness of 87.1 km containing 19.5% of the total bulk amount of HPEs; b) mediumE (case 85), which employs a crust with an average crustal thickness of 62 km containing 67.8% of the total bulk amount of HPEs; c) highE (case 65), which employs a crust with an average crustal thickness of 87.1 km containing 97.6% of the total bulk amount of HPEs. Bottom panels: corresponding S-wave velocity gradient. The mantle compositional model used here is YOS20 (Yoshizaki and McDonough, 2020). Note that the color scale is saturated for the largest S-wave velocity gradient.

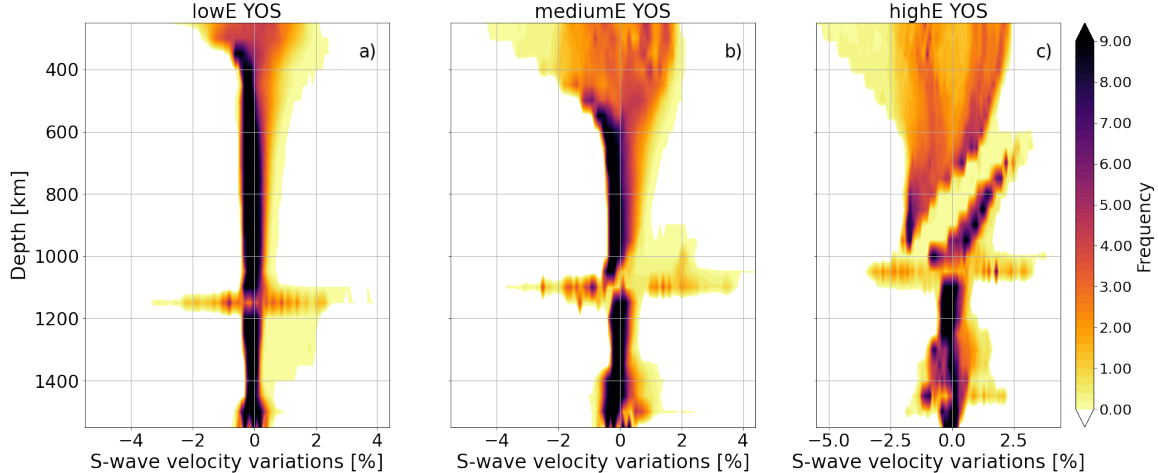


Figure S8: S-wave velocity variations shown as 2D histograms for a) lowE, b) mediumE, and c) highE cases. The histograms have been computed by calculating equal-area histograms at each depth between 250 km and CMB. The colors are proportional to the frequency of the S-wave velocity values at each depth. The mantle compositional model used here is YOS20 *Yoshizaki and McDonough (2020)*.

phase diagrams in the previous section).

Fig. S8 shows 2D histograms of the velocity variations similar to Fig. 5 of the main text, but for the YOS20 composition.

S3 Effects of crustal thickness and crustal enrichment in heat producing elements (HPEs)

In the following, we compare three cases that have different crustal thicknesses but a moderate amount of crustal HPEs, close to the mediumE model. Details about the crustal thickness and crustal radioactivity are listed in Table S1.

The model mLE-tnCr (moderate-low enrichment, thin crust) has an average crustal thickness of 29.5 km. The crust contains in this case 48.2% of the total amount of HPEs. The model mhE-mdCr (moderate-high enrichment, medium crust) has an average crustal thickness of 45 km and contains 55.7% of the bulk amount of HPEs in the crust, while the case mdE-tkCr (moderate enrichment, thick crust) has an average crustal thickness of 48.8 km and 51.8% of the total amount of HPEs in the crust. We note that the models mhE-mdCr and mLE-tnCr use respectively a 20% and 70% larger crustal enrichment in HPEs than suggested by the GRS data (*Hahn et al., 2011*). The models mLE-tnCr, mhE-mdCr, and mdE-tkCr correspond to the cases 126, 110, and 124 of *Plesa et al. (2018)*.

The temperature profiles for these three cases are similar to each other (Fig. S9). For comparison we also show the temperature profile of the mediumE model (average crustal thickness of 62 km containing 67.8% of the bulk HPEs).

Table S1: Summary of crustal thickness and crustal amount of HPEs for cases mlE-tnCr, mhE-mdCr, and mdE-tkCr. For each model we also list the corresponding case number as presented in *Plesa et al. (2018)*, where details on all additional parameters can be found.

| Case id | Crustal thickness [km] | Crustal amount of HPEs [% of total bulk HPE] | Case number <i>Plesa et al. (2018)</i> |
|-----------------------|------------------------|--|--|
| mlE-tnCr ¹ | 29.5 | 48.2 | 126 |
| mhE-mdCr ² | 45 | 55.7 | 110 |
| mdE-tkCr ³ | 48.8 | 51.8 | 124 |

- 1 The crustal heat production rate is 70% higher than the value suggested by the GRS surface data.
- 2 The crustal heat production rate is 20% higher than the value suggested by the GRS surface data.
- 3 This case uses the crustal heat production rate suggested by the GRS surface data.

The velocity variations in the uppermost 700 km are similar for the mlE-tnCr, mhE-mdCr, and mdE-tkCr models (Fig. S10) but with subtle differences. The S-wave velocity variations are slightly more pronounced in case mdE-tkCr, which has the thickest crust of the three models. At 400 km depth, case mdE-tkCr shows the largest local area where the S-wave gradient is positive compared to case mlE-tnCr, where no positive S-wave velocity gradient is observed at the same depth. At 500 km depth only parts of the southern hemisphere show a positive S-wave velocity gradient for case mlE-tnCr, while for case mdE-tkCr a positive S-wave velocity gradient is observed for the entire southern hemisphere. However, in all three cases (mlE-tnCr, mhE-mdCr, and mdE-tkCr), the seismic velocities pattern similar to the crustal thickness distribution is still visible at 400 km depth but not at a depth of 500 km. A negative S-wave velocity gradient is no longer observed for depths of 600 km and deeper (cf. Fig. S9 in Section 2 of the SI). This similarity between these three cases demonstrates that there is a trade-off between the crustal thickness and the crustal enrichment in HPEs. InSight will determine the seismic velocities in the uppermost 600 km to within ± 0.25 km/s (*Smrekar et al., 2019; Lognonné et al., 2012*). In the three cases presented above the mantle seismic velocities and their variations are very similar and will not be distinguishable from each other. However, additional information on the crustal thickness and its variations would help to place constraints on the amount of crustal HPEs.

S4 Low-velocity zones

In Fig. S11 we show the presence of low-velocity zones (LVZ) for the entire set of thermal evolution models and for both TAY13 and YOS20 compositions. Compared to the YOS20 composition, several models using the TAY13 show low-velocity zones located close to the CMB. The presence of a LVZ close to the CMB is observed for cases with cold CMB temperatures. For these cases a larger proportion of garnet and ferropericlasite becomes stable in the lower part of the mantle at the expense of ringwoodite. Additionally the TAY13 composition contains more Fe compared to the YOS20 composition, which affects

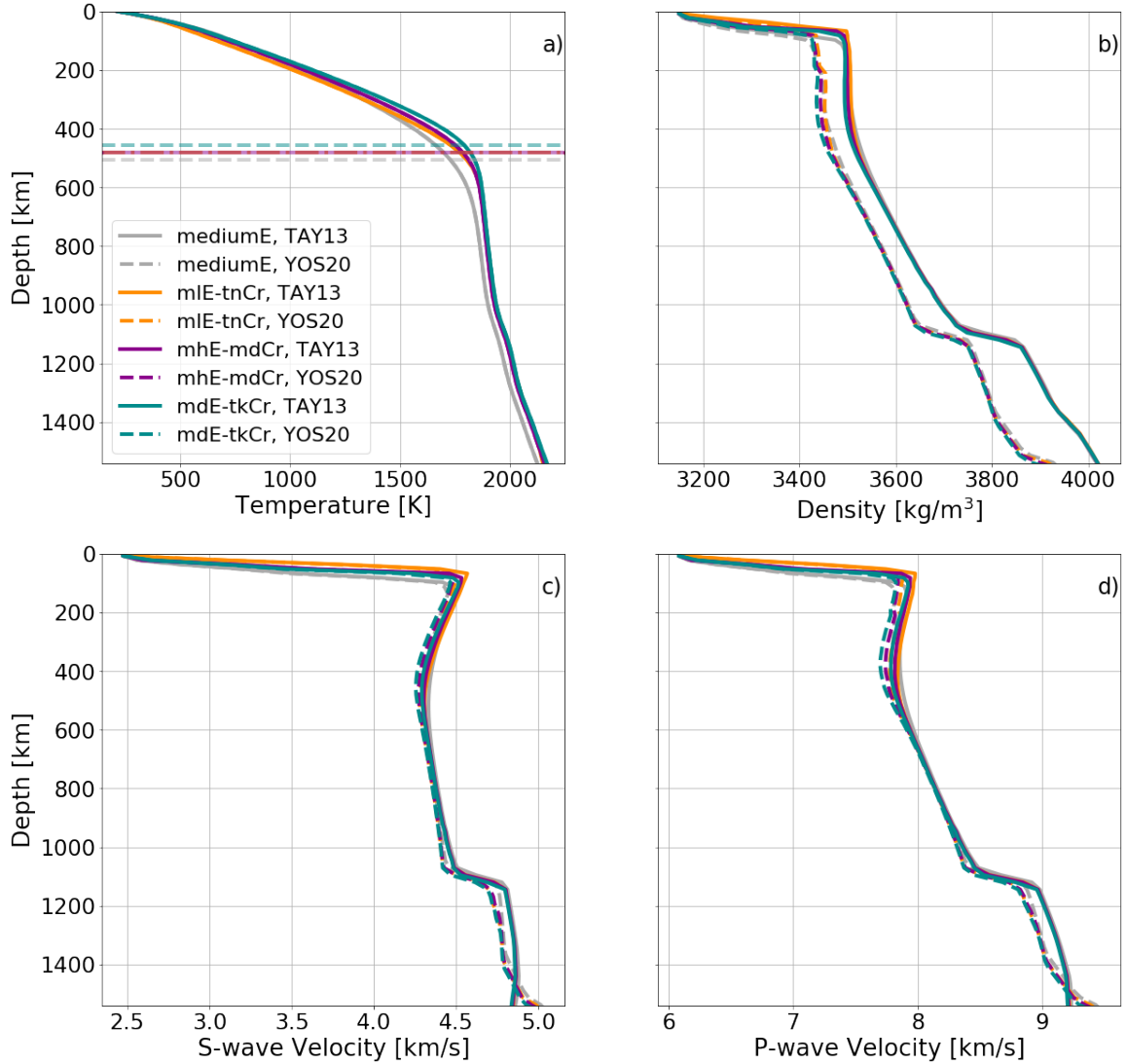


Figure S9: Results of model calculations comparing the mantle composition of Taylor (*Taylor, 2013*) and Yoshizaki (*Yoshizaki and McDonough, 2020*) for the models mlE-tnCr, mhE-mdCr, and mdE-tkCr: a) average temperature profiles; b) average density profiles; c) average S-wave velocity and d) average P-wave velocity profile. The profiles for the mediumE case are also shown for comparison. The average lithosphere thickness of each model is indicated in panel a) by horizontal lines.

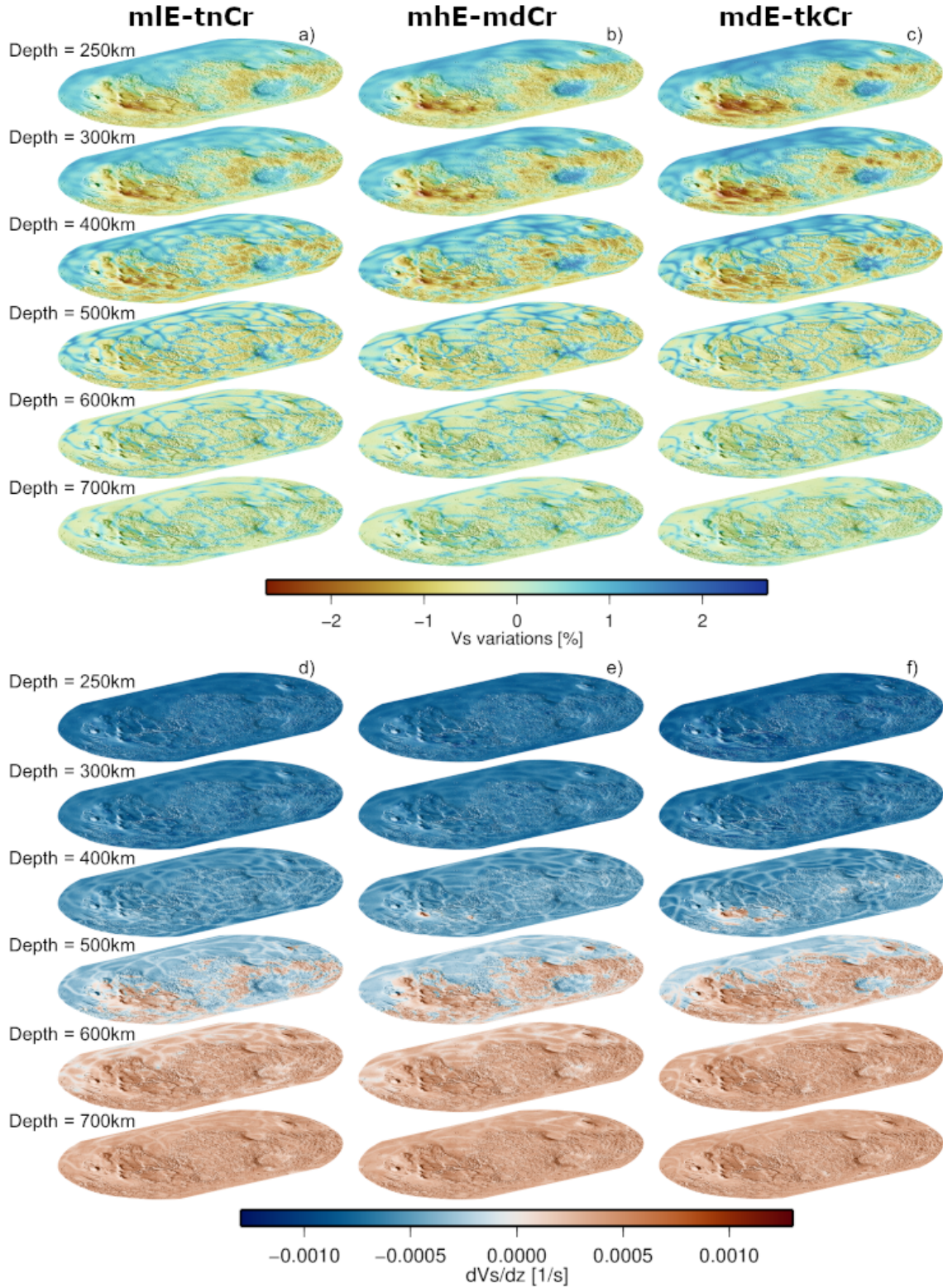


Figure S10: Top panels: seismic velocity variations as a function of depth: a) mIE-tnCr, b) mhE-mdCr, c) mdE-tkCr. Bottom panels: corresponding S-wave velocity gradient. The mantle compositional model used here is TAY13 *Taylor* (2013).

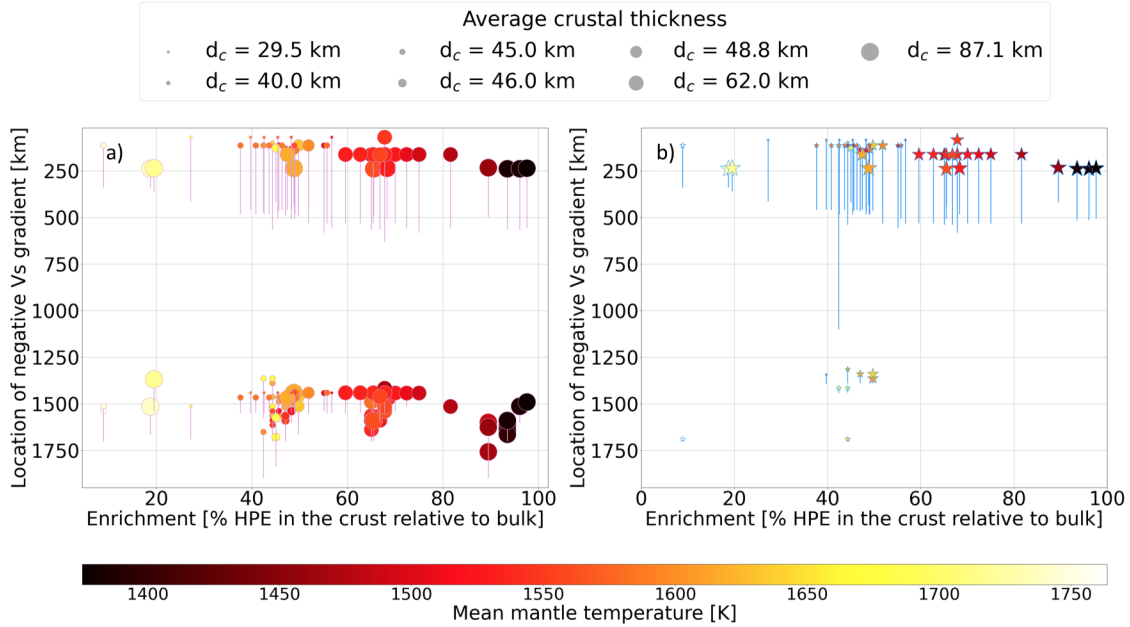


Figure S11: Seismic velocities for 3D thermal evolution models of *Plesa et al.* (2018): a) segments showing the extent of negative V_s gradient region, which have been calculated based on the average V_s profile for the Taylor composition; b) segments showing the extent of negative V_s gradient region, which have been calculated based on the average V_s profile for the Yoshizaki composition.

the S-wave velocity of the stable mineral phases.

S5 Ray tracing calculations for YOS20 composition

Here we show the results of ray tracing calculations for the YOS20 model using the end-member cases (case68, lowE and case65, highE, respectively) and the intermediate case (mediumE, case85).

Similar to the TAY13 composition, the lowE model (case 68) that contains less than 20% of the heat producing elements in the crust shows a shadow zone at epicentral distance between 24° and 37° and is incompatible with the seismic observations by InSight (Fig. S12).

S6 Shadow zone analysis

From a total of 260 models (130 thermal evolution models using two compositions, i.e. TAY13 and YOS20), we find that eight models (cases 22, 23, 24, and 68 using the TAY13 composition, and cases 8, 16, 28, and 68 using the YOS20 composition) have S wave shadow zones in the relevant distance range (i.e., 25° to 35°) when the source depth is located at 50 km. For a source depth located at 100 km cases 22, 23 24 and 57 using the TAY13 composition and cases 5, 22, 24, 57, and 68 using YOS20 composition show shadow zones for at least one of the relevant epicentral distances. For a deeper source located at 150 km the shallow LVZ become less relevant and only two models case 21 and 77 using TAY13

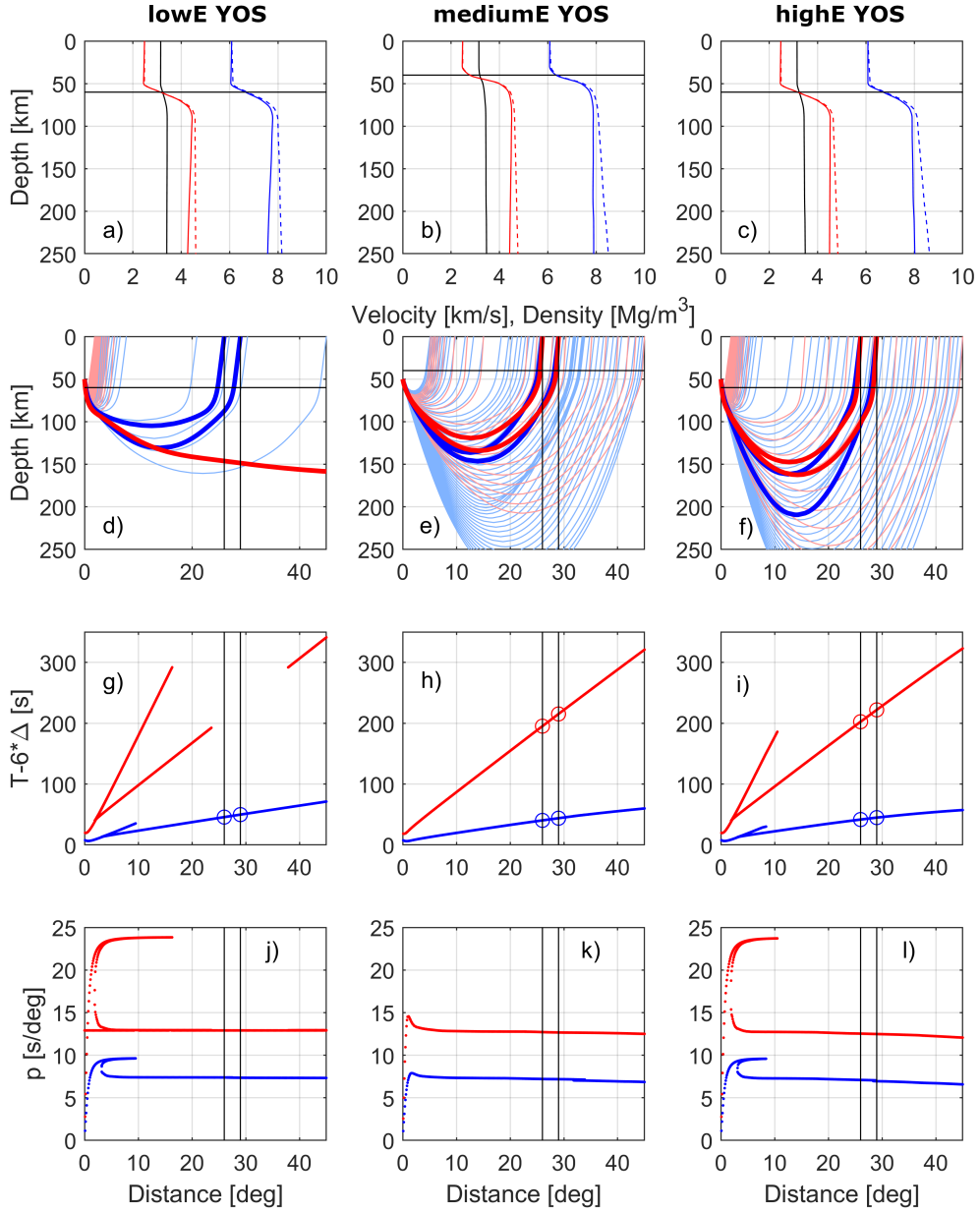


Figure S12: Ray tracing and shadow zone analysis of lowE (case 68, left column), mediumE (case 85, middle column), and highE (case 65, right column) using the YOS20 composition. See main text for details. Note that the S ray for case68 (lowE) in (d), which apparently misses its target distance, actually consists of four rays that arrive at $360^\circ - 26^\circ$, $360^\circ - 29^\circ$, $360^\circ + 26^\circ$, and $360^\circ + 29^\circ$, which, however, yield far too long travel times to be compatible with observed events.

and YOS20, respectively, can be excluded. While cases 22, 23, 24, 57, and 68 of *Plesa et al.* (2018) contain less than 20% of the total amount of HPEs in the crust, cases 16, 21, and 28 employ a low mantle reference viscosity (i.e., $\eta_{ref} < 5 \times 10^{20}$ Pa s). Case 8 has a lower thermal conductivity of the crust compared to other cases ($2 \text{ Wm}^{-1}\text{K}^{-1}$ vs. $3 \text{ Wm}^{-1}\text{K}^{-1}$), and therefore a higher mantle temperature and a higher thermal gradient that in turn leads to shadow zones. Cases 5 and 77 have no specific parameters, but they have thicker mantles and hence smaller cores (case 5 has a mantle thickness $D = 1700$ km, while for case 77, $D = 1900$ km). All these models show a lithosphere thinner than 450 km on average and an average thermal gradient in the lithosphere larger than 3.5 K/km.

S7 Datasets

The following datasets are available on Figshare <https://doi.org/10.6084/m9.figshare.12625703.v1>.

Data Set S1: PerpleX_TAY13_Table.tab

Interpolation table for density and seismic velocities computed using Perple_X for the TAY13 composition *Taylor* (2013).

Data Set S2: PerpleX_YOS20_Table.tab

Interpolation table for density and seismic velocities computed using Perple_X for the YOS20 composition *Yoshizaki and McDonough* (2020).

Data Set S3: Case68_TAY13.txt.zip

3D dataset of density and seismic velocities values obtained for case 68 (lowE) using TAY13 composition.

Data Set S4: Case85_TAY13.txt.zip

3D dataset of density and seismic velocities values obtained for case 85 (mediumE) using TAY13 composition.

Data Set S5: Case65_TAY13.txt.zip

3D dataset of density and seismic velocities values obtained for case 65 (highE) using TAY13 composition.

Data Set S6: Case68_YOS20.txt.zip

3D dataset of density and seismic velocities values obtained for case 68 (lowE) using YOS20 composition.

Data Set S7: Case85_YOS20.txt.zip

3D dataset of density and seismic velocities values obtained for case 85 (mediumE) using YOS20 composition.

Data Set S8: Case65_YOS20.txt.zip

3D dataset of density and seismic velocities values obtained for case 65 (highE) using YOS20 composition.

Data Set S9: ShadowZones_50km.csv

Shadow zone calculations for TAY13 and YOS20 compositions and a source depth located at 50 km. P/ct. P shows the relative number of P waves arriving at epicentral distance range of 25°–30° compared to a constant velocity model. Similarly, S/ct. S shows the relative number of S waves compared to a constant velocity model, while S/P calculates the relative number of S waves compared to P waves arriving at the same epicentral distance range. The numbers given for Shadow P and Shadow S show where both epicentral distances of S0173a and S0235b (2), just one of them (1) or none of them (0) could be reached.

Data Set S10: ShadowZones_100km.csv

Similar to Data Set S9 but for a source depth of 100 km.

Data Set S11: ShadowZones_150km.csv

Similar to Data Set S9 but for a source depth of 150 km.

References

- Hahn, B. C., S. M. McLennan, and E. C. Klein, Martian surface heat production and crustal heat flow from Mars Odyssey Gamma-Ray spectrometry, *Geophysical Research Letters*, 38(14), doi:10.1029/2011GL047435, 2011.
- Lognonné, P., W. Banerdt, K. Hurst, D. Mimoun, R. Garcia, M. Lefeuvre, J. Gagnepain-Beyneix, M. Wieczorek, A. Mocquet, M. Panning, et al., Insight and single-station broadband seismology: from signal and noise to interior structure determination, *LPI*, (1659), 1983, 2012.
- Plesa, A.-C., S. Padovan, N. Tosi, D. Breuer, M. Grott, M. Wieczorek, T. Spohn, S. Smrekar, and W. Banerdt, The thermal state and interior structure of Mars, *Geophysical Research Letters*, 45(22), 12–198, 2018.
- Smrekar, S. E., P. Lognonné, T. Spohn, W. B. Banerdt, D. Breuer, U. Christensen, V. Dehant, M. Drilleau, W. Folkner, N. Fuji, et al., Pre-mission InSights on the Interior of Mars, *Space Science Reviews*, 215(1), 3, 2019.
- Stixrude, L., and C. Lithgow-Bertelloni, Thermodynamics of mantle minerals-II. Phase equilibria, *Geophysical Journal International*, 184(3), 1180–1213, 2011.
- Taylor, G. J., The bulk composition of Mars, *Geochemistry*, 73(4), 401–420, 2013.
- Taylor, S. R., and S. McLennan, *Planetary crusts: their composition, origin and evolution*, 378 pp., Cambridge University Press, 2009.
- Yoshizaki, T., and W. F. McDonough, The composition of Mars, *Geochimica et Cosmochimica Acta*, 273, 137–162, 2020.